Long-period surface motion of the multipatch M_w9.0 Tohoku-Oki earthquake

Panos A. Psimoulis,[1,2] Nicolas Houlié,[2,3] Clotaire Michel,[4] Michael Meindl[2] and Markus Rothacher[2]

[1]*Department of Civil Engineering, Nottingham Geospatial Institute, The University of Nottingham, Nottingham, NG7 2TU, United Kingdom.*
E-mail: panagiotis.psimoulis@nottingham.ac.uk
[2]*Geodesy and Geodynamics Lab., Institute of Geodesy and Photogrammetry, ETH Zurich, Zurich 8093, Switzerland*
[3]*Seismology and Geodynamics, Institute of Geophysics, ETH Zurich, Zurich 8092, Switzerland*
[4]*Swiss Seismological Service, ETH Zurich, Zurich 8092, Switzerland*

SUMMARY

We show that it is possible to capture the oscillatory ground motion induced by the Tohoku-Oki event for periods ranging from 3 to 100 s using precise point positioning. We find that the ground motions of the sedimentary basins of Japan were large (respectively >0.15 m s^{-1} and >0.15 m s^{-2} for velocity and acceleration) even for periods larger than 3 s. We compare geodetic observables with a ground motion prediction equation designed for Japan seismicity and find that the spectral acceleration is well estimated for periods larger than 3 s and distances ranging from 100 to 500 km. At last, through the analysis of the displacement attenuation plots, we show that the 2011 Tohoku-Oki event is likely composed of multiple rupture patches as suggested before by time-reversal inversions of seismic data.

Key words: Satellite geodesy; Transient deformation; Earthquake ground motions; Surface waves and free oscillations; Early warning.

1 INTRODUCTION

For solid Earth investigation, high-rate GPS is nowadays an essential tool in the study of transient deformation, seismic source at depth, or accurate determination of strain rate and surface velocity fields. In the field of engineering, high-rate GPS is used to determine the deformation or the motion of structures (bridges, high buildings, etc.) in time (Çelebi & Sanli 2002; Psimoulis *et al.* 2008). Koketsu & Miyake (2008) showed that long-period ground motion is also of interest for the increasing number of large civil engineering structures such as bridges and tall buildings since far-distance resonance and short-distance directivity could occur. In the current study we investigate whether GPS is reliable and accurate in the determination of oscillatory ground motions (acceleration, velocity and displacement) for frequencies lower than or equal to 0.33 Hz.

Peak ground accelerations and velocities (PGA, PGV) are routinely computed using seismic data in near real-time (minutes or less) in the 0.5–25 Hz frequency range (typically) in order to assess the possible consequences of an earthquake shortly after its occurrence. The relationship between magnitude and peak ground motions of an event is distorted by the interaction between seismic waves and the structures (sedimentary basins, fault systems, etc.) sampled during their travel from the source (e.g. Roten *et al.* 2011 or Denolle *et al.* 2013). Ground motion prediction equations (GMPEs) predict that the peak motions representative of longer periods,

such as the spectral acceleration (SA) at 3 s depend proportionally more on the event's magnitudes than PGA or PGV (e.g. Zhao *et al.* 2006). Nevertheless, few GMPEs for peak motions representative of long-periods are available in the literature due to the limited amount of broadband data (Cauzzi & Faccioli 2008). For this reason, peak ground displacements (PGDs) are generally not available and proxies like the displacement response spectrum (DRS; 10 s) are used (Cauzzi & Faccioli 2008). We explore whether GPS can contribute to GMPEs but also if the seismic source can be better characterized using long-period surface oscillatory motions.

As seismic waveforms, GPS time-series provide insights into surface transients observed during seismic wave propagation or during a seismic rupture (Larson *et al.* 2003; Bock *et al.* 2004, 2011; Ji *et al.* 2004; Miyazaki *et al.* 2004; Blewitt *et al.* 2006; Kobayashi *et al.* 2006; Ohta *et al.* 2006, 2012; Emore *et al.* 2007; Wang *et al.* 2007; Yokota *et al.* 2009; Delouis *et al.* 2010; Feng *et al.* 2010; Avallone *et al.* 2011; Houlié *et al.* 2011; Mitsui & Heki 2012; Wright *et al.* 2012; Guo *et al.* 2013; Meng *et al.* 2013; Houlié *et al.* 2014; Psimoulis *et al.* 2015), tsunami generation for early warning (Blewitt *et al.* 2006, 2009; Sobolev *et al.* 2007; Crowell *et al.* 2009; Behrens *et al.* 2010; Ohta *et al.* 2012; Li *et al.* 2013a), changes in ionosphere status (Ducic *et al.* 2003; Mai & Kian 2009; Galvan *et al.* 2012; Karia *et al.* 2012), volcanic plumes (Houlié *et al.* 2005, 2006; Newman *et al.* 2012), water vapour delays (Perler *et al.* 2011; Hurter *et al.* 2012), or moment tensor (O'Toole *et al.* 2012,
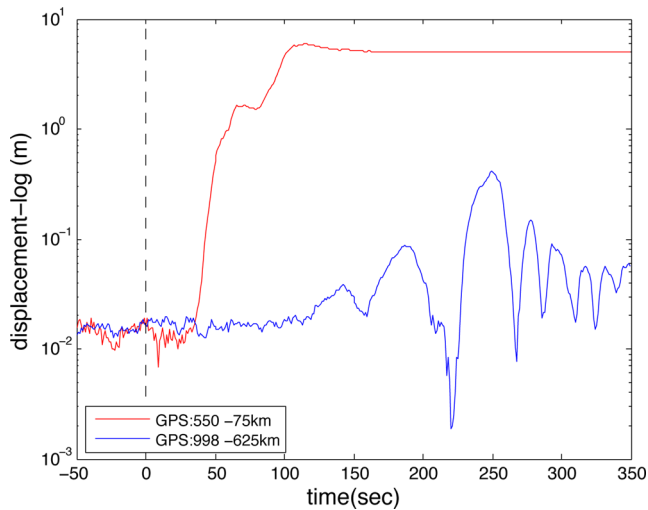
Figure 1. The EW displacement time-series for the GPS site closest to the epicentre (GPS 0550; ∼75 km away) and for a remote site (GPS 0998; ∼650 km); time origin corresponds to the earthquake occurrence. The time difference between the two responses reflects the delay of the arrival of the seismic signal at the station far from the epicentre.

2013). However, apart from few exceptions (i.e. see Ohta *et al.* 2012; Wright *et al.* 2012), the studies listed above did not make use of real-time or near real-time data processing strategies. Precise point positioning (PPP) allows to monitor the motion of standalone GPS sites (Blewitt 2008; Ge *et al.* 2008; Jokinen *et al.* 2013). GPS, which is accurate up to a few millimetres for high-frequency oscillations in differential mode (Psimoulis & Stiros 2008, 2012), is accurate at the centimetre level in PPP mode (Moschas *et al.* 2014), accuracy which is sufficient to determine the surface displacement (Fig. 1) following large events ($M_w > 7.0$). The PPP GPS time-series have not been used until today as a tool to describe the surface oscillatory motion. In this study, we propose to use PPP time-series processed for the GEONET continuous GPS (CGPS) sites to study the ground motions that followed the 2011 Tohoku-Oki event.

The Tohoku-Oki event (origin time T_0 at 05:46:23 UTC on 2011 March 11) and the subsequent tsunami stroke Japan with a heavy impact on structures. The rupture area is exceptionally compact for such magnitude (∼M_w9.0 and $L \sim 500$ km, to be compared with the 1000 km of rupture of the 2004 Sumatra event with a similar magnitude, Vigny *et al.* 2005) with most of the slip contained above 30 km depth and a maximum slip on the fault of nearly 50 m (Koketsu *et al.* 2011; Suzuki *et al.* 2011; Yagi & Fukahata 2011; Yue & Lay 2011). Because of the poor coverage near the epicentre, the slip distribution near the surface is not well constrained. Other studies (Maercklin *et al.* 2012; Roten *et al.* 2012) confirmed that the long-period (10–20 s) maximum slip was up to 50 m but also suggested that the Tohoku-Oki event was indeed composed of multiple ruptures of smaller magnitudes ($<M_w$8.8).

2 DATA

2.1 GPS data

The M_w9.0 earthquake off the Pacific coast of Tohoku-Oki on 2011 March 11 was fully recorded by the GEONET network (Sagiya 2004), operated by the Geospatial Information Authority of Japan (GSI). The GEONET network is composed of over 1200 continuously observing GPS receivers (with an average spacing of 20
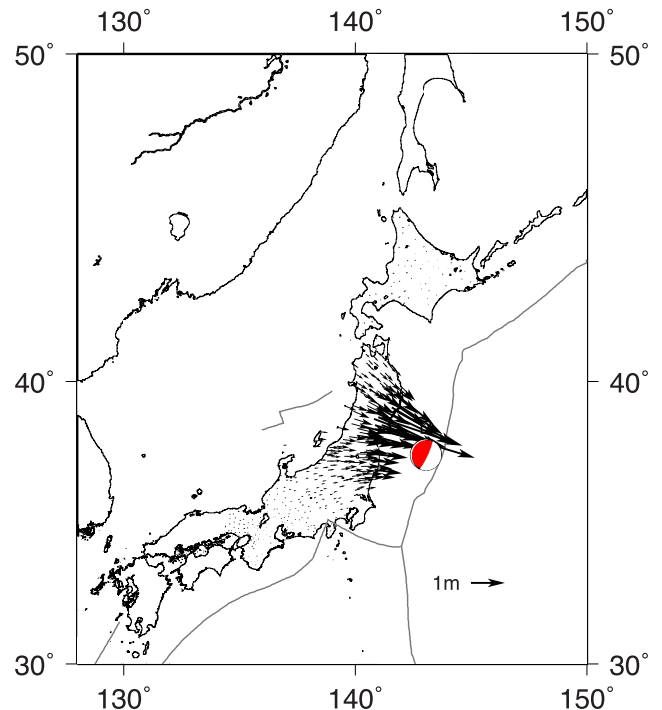

Figure 2. Precise point positioning (PPP) coseismic horizontal displacement field for the Tohoku-Oki event measured by the GEONET GPS network at $t = T_0 + 300$ s.

km). We processed 1 Hz GPS records from 847 GEONET stations of 15-hr duration, fully covering the earthquake period. The data was analysed with the Bernese GPS Software (Dach *et al.* 2007). The data were post-processed in a PPP mode using state-of-the-art models and a-priori information of highest quality from the Center for Orbit Determination in Europe (Bock *et al.* 2009; Dach *et al.* 2009). As an example for the results obtained, Fig. 2 shows the displacement field at 300 s after the origin time (T_0). The displacement time-series in North, East, and vertical components were established separately for each station. The GPS displacement time-series show an *a posteriori* formal accuracy of about 1 cm in the horizontal and 2 cm in the vertical component, respectively (Psimoulis *et al.* 2015).

2.2 Strong motion data

The largest strong-motion networks of Japan called K-NET (Kyoshin network) and KiK-net (Kiban-Kyoshin network) consist of 1034 and 660 stations, respectively (Aoi *et al.* 2011). The main difference of the two networks is that the K-NET stations are located mainly on thick sedimentary sites, while the KiK-net stations are deployed on rock or thin sedimentary sites, as it is a subnet of the Hi-net (high-sensitivity seismograph network) primarily designed for highly sensitive seismic observations. Consequently, the K-NET and KiK-net triggering thresholds are different (2 and 0.2 cm s^{-2}, Aoi *et al.* 2004). Furthermore, the K-NET stations are installed on the ground surface, while each KiK-net site hosts two instruments, one installed at the surface and the second at the bottom of a borehole of 100–200 m depth.

The M_w9.0 earthquake of Tohoku-Oki 2011 was well recorded by the two strong-motion networks. Raw data of strong-motion records from 700 K-NET sites and 525 KiK-net sites were available. The records of three components, corresponding to the north, east and vertical directions, were sampled at 100 Hz and up to 300 s duration. The acceleration of each site was derived by correcting the raw
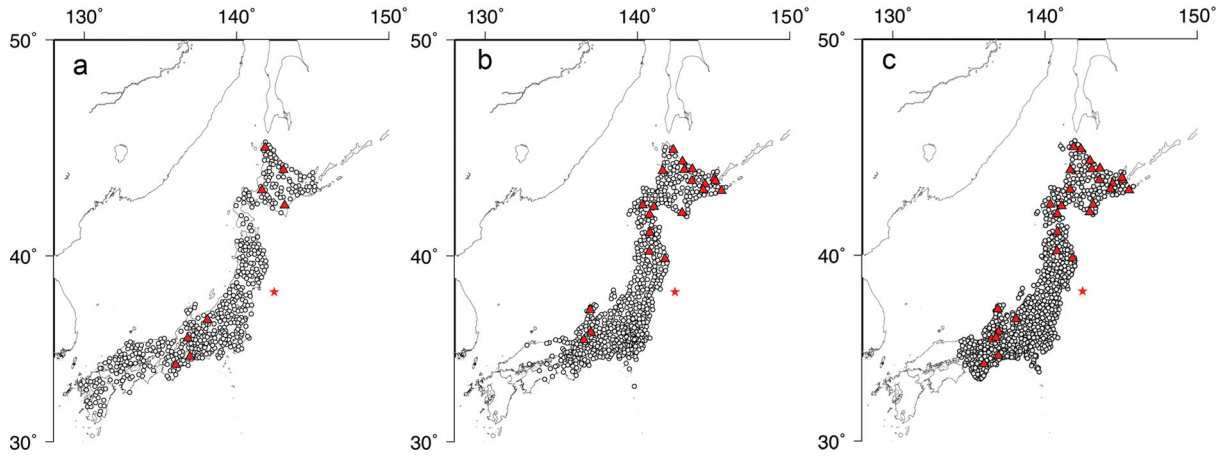
Figure 3. KiK-net (a), K-NET (b) and GEONET GPS (c) sites used in this study. The very closely located sites of GPS and strong-motion networks are indicated with red triangles. The red star indicates the epicentre of the Tohoku-Oki earthquake in 2011.

Table 1. The closely located GPS and strong-motion sites of K-NET and KiK-net with their location (latitude, longitude) and distance from the epicentre.

GPS	K-NET	KiK-net	Latitude (°)	Longitude (°)	Sensor distance (m)	Epicentre distance (km)
0005	HKD080	–	43.50786	144.44901	45	604
0041	FKS011	–	37.09071	140.90252	97	186
0115	HKD066	–	43.66182	145.13143	20	639
0122	HKD083	–	43.23294	144.32503	20	572
0140	HKD151	–	42.49436	140.35420	25	496
0144	HKD110	–	42.13094	142.93539	39	428
0147	HKD155	–	42.04297	140.80554	99	436
0164	IWT019	–	39.84918	141.80385	39	179
0183	AKT006	–	40.21544	140.78733	26	253
0280	GIF006	–	36.03305	136.95276	28	541
0285	GIF012	–	35.63615	136.48877	64	600
0502	HKD043	–	44.58204	142.96446	6	700
0503	HKD048	–	44.21972	143.61567	24	666
0504	–	ABSH04	44.19194	143.07682	12	657
0511	HKD056	–	43.67050	143.57815	25	605
0519	HKD072	–	43.19517	145.52050	52	605
0535	AOM027	–	41.14555	140.82198	29	343
0779	HKD006	–	45.12678	142.35184	21	758
0783	HKD020	–	44.14876	141.66460	37	652
0792	HKD131	–	42.42055	141.08106	67	471
0793	–	TKCH08	42.48641	143.15197	10	470
0849	–	SOYH04	45.23011	141.88178	95	771
0864	HKD065	–	43.79403	145.05686	39	650
0877	–	IKRH02	43.22090	141.65202	60	550
0972	ISK015	–	37.22644	136.90877	9	494
0983	–	NGNH28	36.70665	138.09673	99	416
0991	–	GIFH23	35.72349	136.78462	7	572
0998	–	AICH21	34.74005	136.93848	6	625
1009	–	NARH03	34.29293	136.00264	63	723

data for the gain, converting the corresponding record time from UTC to GPS time and then by applying the time correction for 15 leap seconds. In order to be consistent with the recorded motion of the GPS and K-NET sites, only KiK-net surface records were investigated in this study.

3 RESULTS

3.1 Consistency of GPS and strong-motion data

The evaluation of the consistency of GPS and strong-motion records at high frequencies must be completed for sites located very closely.

In previous studies, the GPS and strong-motion sites with an interdistance of less than 1 km were assumed as collocated (Melgar *et al.* 2013). In our study, we used an even more conservative approach by using only the very closely located GPS and strong-motion sites, with an interdistance less than 100 m. In total, we identified 29 very closely located sites of the GPS and strong-motion networks (Fig. 3), comprising 21 K-NET and 8 KiK-net sites (Table 1).

For these sites we assume that the GPS and strong-motion records are not shifted by a significant time difference (<1 s), keeping in mind that the sampling rate (1 Hz) of the GPS network is low compared to the sampling rate of the strong-motion network (100 Hz).
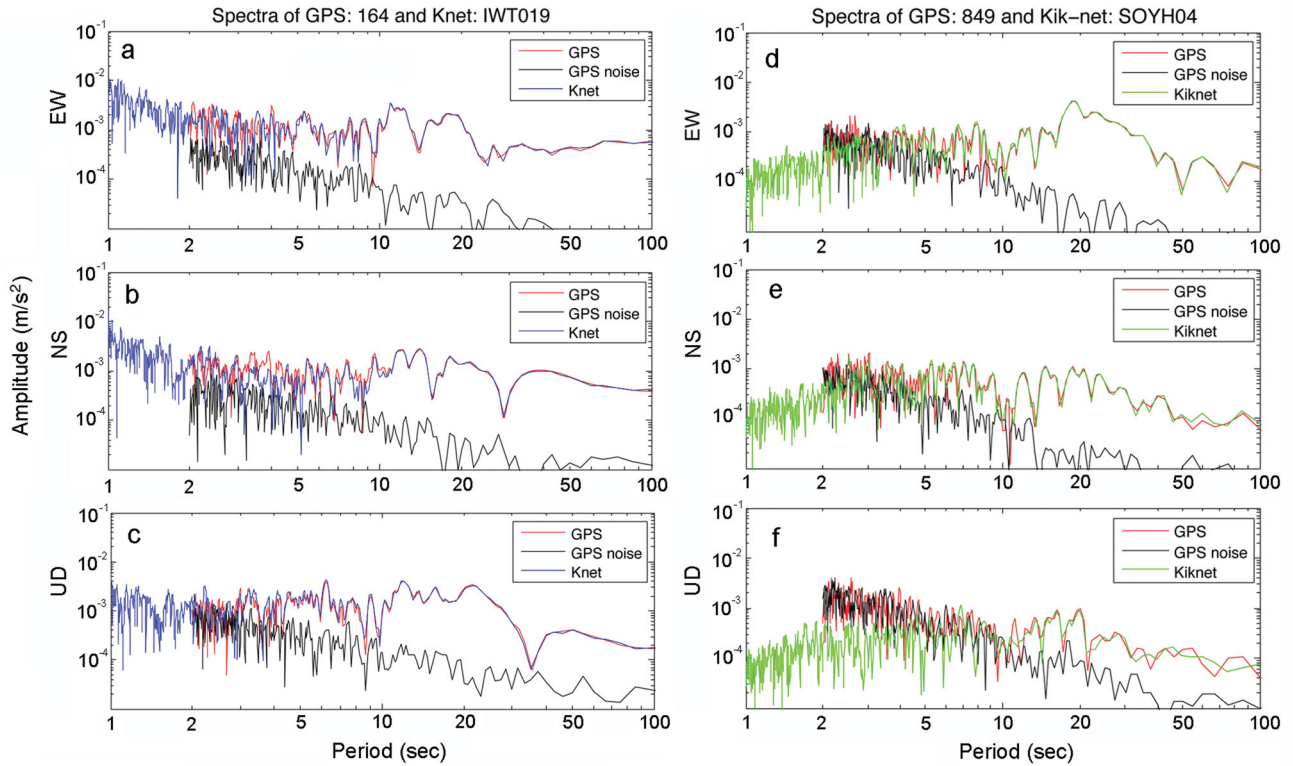
Figure 4. Spectra of derived acceleration time-series using K-NET, KiK-net and GPS data for two sites: (a–c) close (179 km) and (d–f) far (771 km) from the epicentre. The solid black line corresponds to the spectra of the GPS acceleration time-series before the occurrence of the earthquake indicating the noise level.
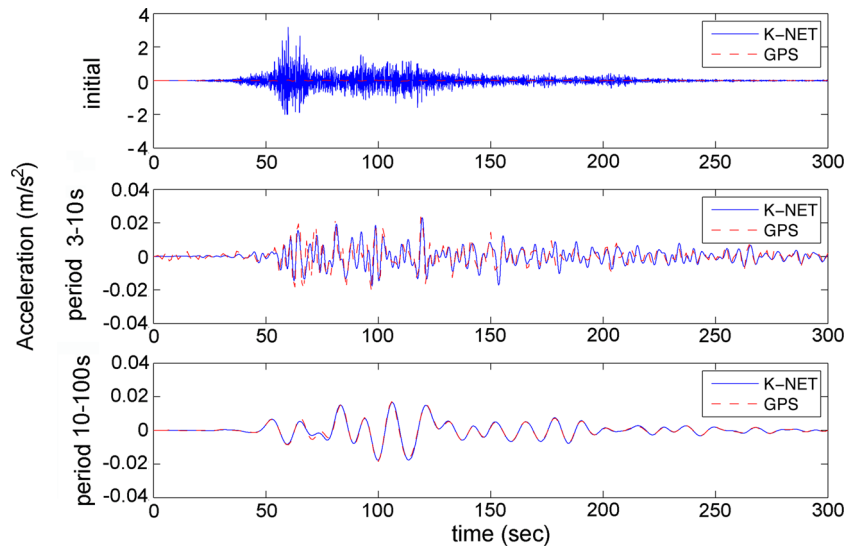

Figure 5. The initial acceleration time-series of the very closely located sites of K-NET IWT019 (blue solid line) and GPS 0164 (dashed red line) and the derived time-series after filtering for the 3–10 and 10–100 s period bands. The time corresponds to seconds since the earthquake occurrence.

The evaluation of the consistency of the GPS and the strong-motion sensors was examined by comparing the spectra of the two records and assessing them in their common frequency range (0–0.5 Hz). The usual technique of integration of strong-motion records for the computation of velocities and displacements was not followed due to the significant accumulated error (Stiros 2008), the large duration of the strong-motion records (up to 300 s) and the significant coseismic displacement (up to 2–3 m), which would make the estimation of the long-period displacement time-series unreliable (Boore 2003).

Thus, instead of integrating the strong-motion records, the GPS displacement series were differentiated twice resulting in acceleration time-series. The derived accelerations are affected also by errors due to the differentiation, which, however, do not accumulate. These differentiation errors affect mainly the short-period acceleration (2–3 s), due to the high short-period noise of GPS measurements relatively to the short time step of the differentiation. Furthermore, the error of the derived accelerations is expected to be higher for the vertical component due to the higher noise level of the corresponding PPP results.

In Fig. 4, we present the spectra of the GPS and the K-NET acceleration time-series of the east–west (EW), north–south (NS) and up–down (UD) components for two representative closely located sites, one close (179 km; Figs 4a–c) and one far (771 km; Figs 4d–f) from the epicentre. In addition, the spectra of the GPS acceleration time-series, corresponding to the time interval before the seismic event, are shown in Fig. 4 as black lines. These spectra provide information on the basic noise of the acceleration time-series derived from GPS. For periods above 3–4 s, the GPS noise is lower than the seismic signal for the horizontal component. This supports the consistency of GPS and K-NET spectra (Figs 4a–c) mainly for periods above 3 s, while KiK-net strong-motion spectra prove to be slightly less consistent (Figs 4d–f) for the periods below 5 s. This is the case in general for sites far from the epicentre (>600 km) where the seismic signal is weak relative to the PPP noise and the S/N decreases, especially for short-periods (<5 s) and for the vertical component (period <10 s). However, such phenomena do not affect this study, as it is focusing on the use of the horizontal components and long-periodic oscillations (>3 s), which usually are not included in the ground motion parameters computation.

3.2 Computation of MGA, MGV and MGD

The maximum ground acceleration (MGA), velocity (MGV) and displacement (MGD) were computed from GPS and strong-motion records for short- (3–10 s) and long-period (10–100 s) domains. The strong-motion records were integrated once and twice into velocities and displacements and the GPS records were differentiated once and twice to obtain velocities and accelerations. The derived strong-motion and GPS time-series were filtered for a short- (3–10 s) and a long-period (10–100 s) band. Fig. 5 shows the acceleration time-series of the GPS and strong-motion instruments that are closely located for the two period bands. For each type of sensor, we compute the absolute maxima (corresponding to MGA, MGV and MGD) of acceleration, velocity, and displacement time-series of every site of each network. Figs 6(a)–(c) show the MGA, MGV and MGD maps for the two period bands. As expected, by comparing the GPS and the strong-motion networks, GPS seems to be more sensitive to long-period ground displacements and the strong-motion sensors to short-period accelerations.

The noise of the GPS acceleration, velocity and displacement time-series was estimated by analysing the time interval before the seismic event, where all the sites are assumed not to be affected by motions. Following the methodology of MGA, MGV and MGD, the GPS noise displacement time-series were differentiated once and twice and subsequently filtered for the two period bands (3–10 and 10–100 s). The maximum value of each resulting time-series expresses the maximum noise level for each GPS site and for each quantity (acceleration, velocity and displacement). In Table 2 the mean average and the standard deviation of the estimated maximum noise values for the horizontal component and for the two examined period bands are listed. All the estimated MGA, MGV and MGD values of the GPS sites are above their respective uncertainty maxima, with the latter computed as the mean maximum error + 3σ zone (2.0 cm s^{-2}, 1.5 cm s^{-1} and 1.0 cm, Fig. 7). The level of the estimated maximum noise is smaller than that in other studies (e.g. Wright *et al.* 2012), due to the limitation of the noise level by filtering the GPS time-series for specific period bands.

The qualitative examination of Fig. 6 shows that strong-motion and GPS provide a consistent estimation of MGA, MGV and MGD
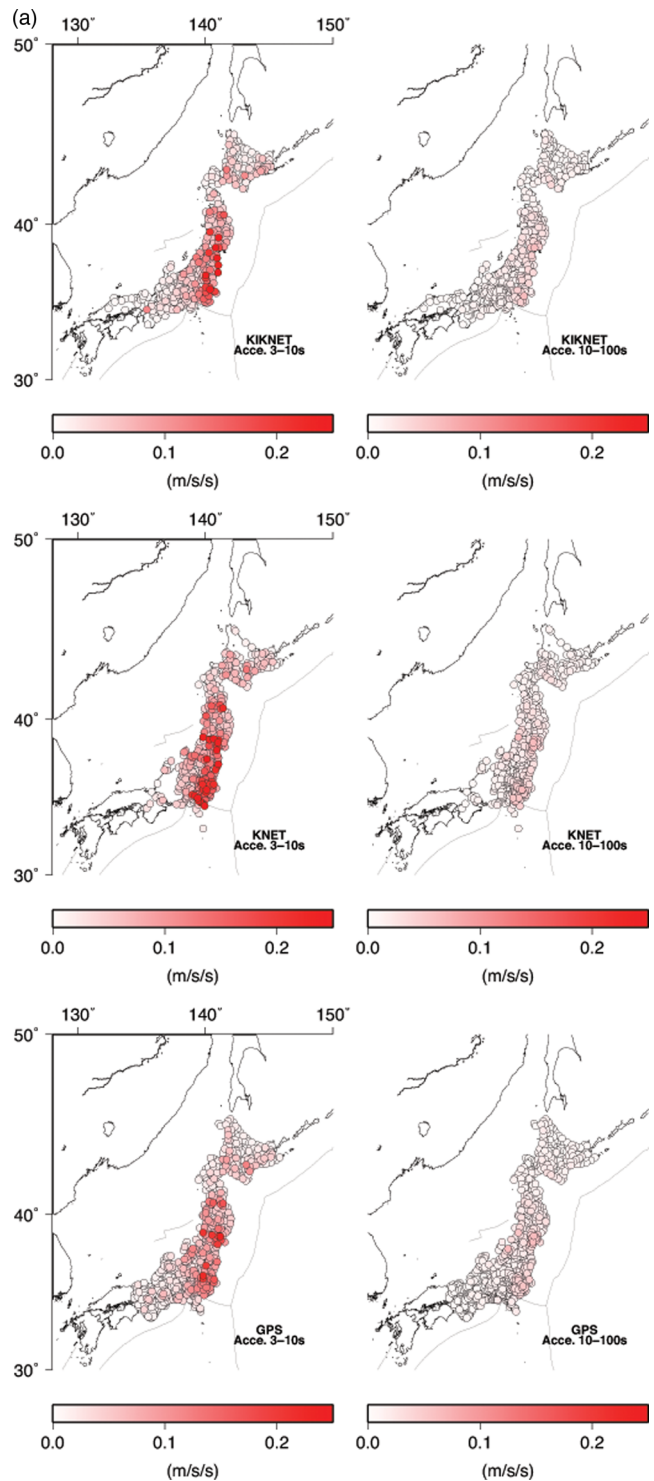

Figure 6. (a) Maximum ground acceleration maps for KiK-net (top), K-NET (middle), and GPS (bottom) for the two period bands (3–10 and 10–100 s). (b) Maximum ground velocity maps for KiK-net (top), K-NET (middle) and GPS (bottom) for the two period bands (3–10 and 10–100 s). (c) Maximum ground displacement maps for KiK-net (top panel), K-NET (middle panel) and GPS (bottom panel) for the two period bands (3–10 and 10–100 s). Note the different scale of the 10–100 s band.
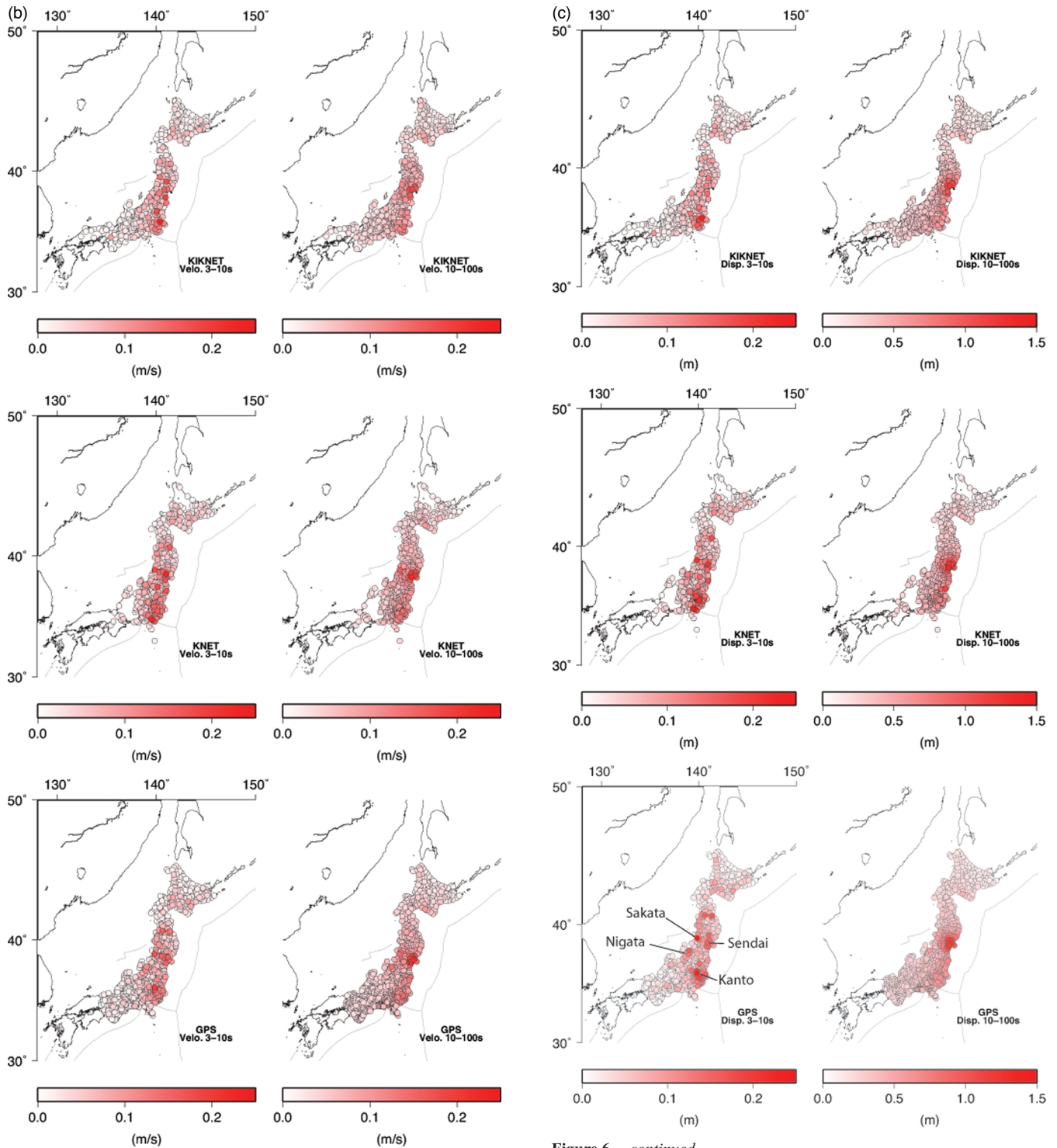
Figure 6 – *continued*


Figure 6 – *continued*

for the two examined period domains. Some local differences for the short-period band might reflect weaknesses of GPS in estimating acceleration of low periods (<4–5 s) or local effects, without disturbing though the overall compatibility of the MGA maps.

At long-periods, the maximum displacement map (Fig. 6c, right-hand side) is smooth and reflects the distance to the largest slip patch on the fault: the maximum values occur close to the epicentre in the Sendai region with large values along the coast to the South.

However, in the 3–10 s band (Figs 6b and c, left-hand side), the map is more complex and highlights large sedimentary basins. In addition to the Sendai basin, close to the epicentre, the largest values are found in the Kanto plain, known to exhibit resonance frequencies in this band (Yamanaka *et al.* 1989). On the western coast, large values can also be found at the Sakata and Niigata basins, in relation with the large amplification in these frequency band as shown by Mamula *et al.* (1984).

Table 2. Mean average and standard deviation of the estimated maximum noise values of the displacements, velocities and accelerations derived from the PPP time-series for the two examined period bands.

	Period 3–10 s		Period 10–100 s	
	Mean average	Standard deviation	Mean average	Standard deviation
Displacement (mm)	4.5	2.3	5.1	2.1
Velocity (mm s^{-1})	5.5	2.7	1.5	0.9
Acceleration (mm s^{-2})	7.6	4.0	1.0	0.7
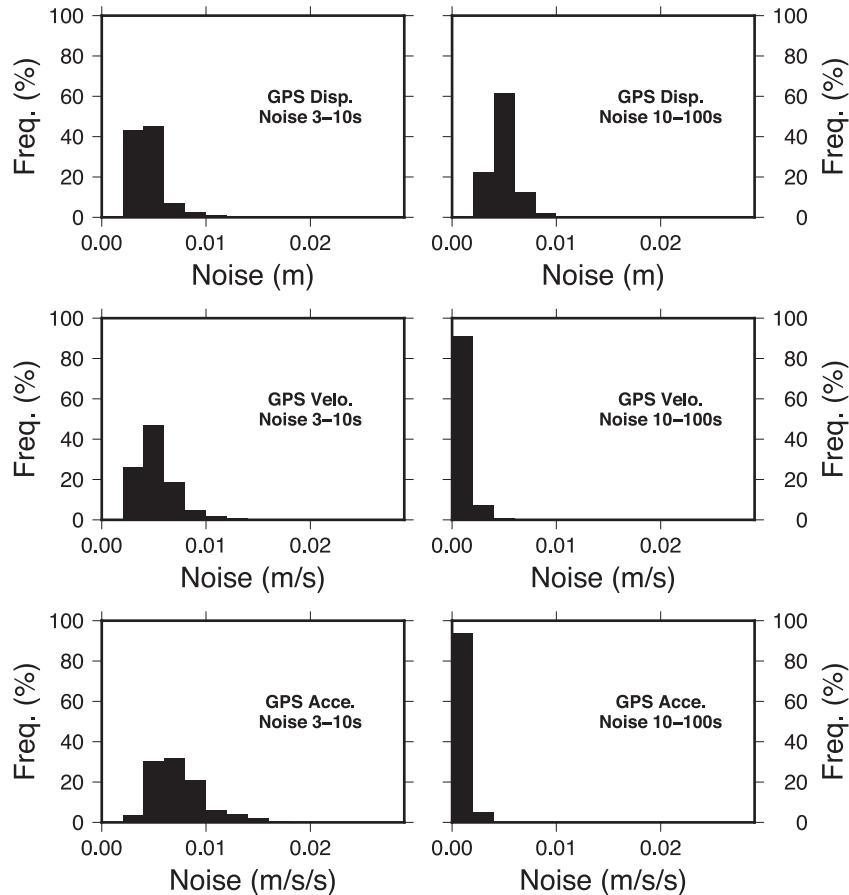
Figure 7. Maximum level of noise derived from the GPS acceleration, velocity and displacement records.

In Fig. 8, we show the differences of the estimated GPS and strong-motion MGA, MGV and MGD for the very closely located sites, normalized to the maximum acceleration, velocity and displacement of the corresponding site. The derived normalized differences show the good agreement between the solutions of GPS and the strong-motion sensors (relative errors mostly below 10 per cent) with the exception the short-period (3–10 s) MGA and MGD differences. The latter are observed mainly for large distances from the epicentre and they are caused by the relatively small oscillatory amplitude of the corresponding accelerations and displacements (up to 0.15 m s^{-2} and 0.10 m, respectively). This can be seen more clearly from the absolute differences of the estimated MGA, MGV and MGD between the GPS and strong-motion sensors in Fig. A1, which reveals the small values (<0.03 cm s^{-2}, <0.03 cm s^{-1}

and 0.05 cm, respectively) for the sites located mainly far from the epicentre. The relatively high differences in the displacement (>3 cm) of some sites far from the epicentre (K-NET GIF006 - GPS 0280, K-NET ISK015 - GPS 0972, K-NET HKD043 - GPS 0502 and K-NET HKD046 - GPS 0504) may be attributed to local effects.

Since we find a general agreement of the GPS records with the seismic data in space and frequency, we compute the SA at 3 s for a 5 per cent damping (Fig. 9). In general the long-period signals are not of concern for the safety of typical building or small objects at the surface. However, a large object such as a bridge, a skyscraper or a deep basin might resonate at long-periods, particularly in the 3–10 s range (Anderson *et al.* 1986; Singh *et al.* 1988; Chávez-García & Bard 1994; Lermo & Chavez-Garcia 1994). Even more rigid
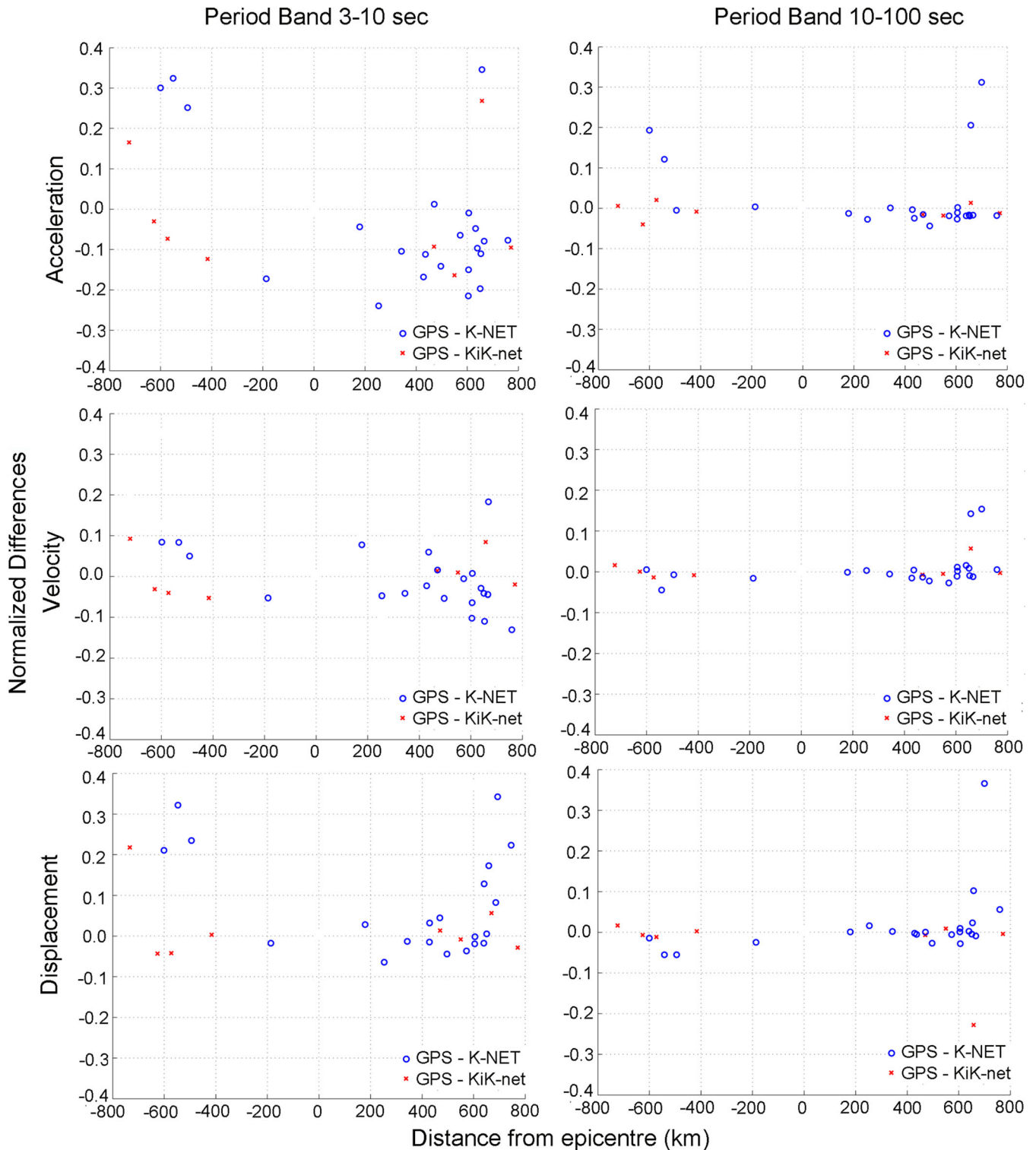
Figure 8. Normalized differences of GPS and strong-motion MGA (top panel), MGV (middle panel) and MGD (bottom panel) at the very closely located sites. The positive and negative distances correspond to the position of the sites northward and southward from the epicentre.

structures might be affected by these long-periods due to site effects, soil-structure interaction and liquefaction (Margaris *et al.* 2010; Assimaki *et al.* 2012). In order to have a baseline in this study, the attenuation of ground motion with distance (SA and acceleration) is compared to the GMPE proposed for Japan by Zhao *et al.* (2006).

Please note that we use the distance from the epicentre (as computed by USGS) whereas Zhao *et al.* (2006) assume the shortest distance between a rupture model and the station. We find that SA (3 s) estimates from GPS and strong-motion data are compatible with maximum values predicted by the GMPE (Fig. 9).
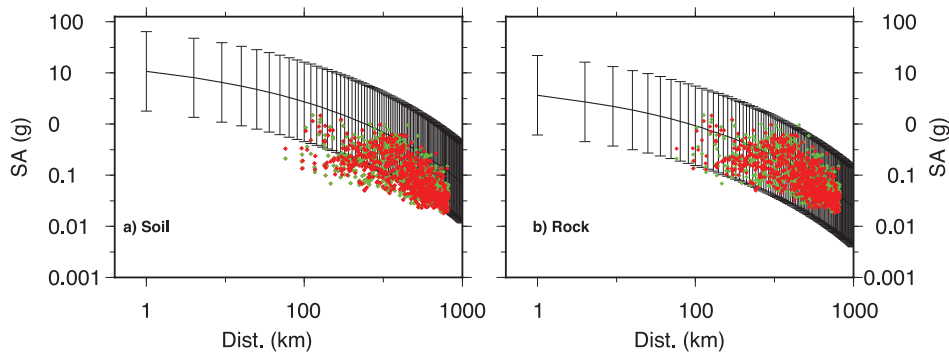
Figure 9. Spectral acceleration (SA) at 3 s from GMPE (black line) of soft soil (a) and bedrock (b) conditions (Zhao *et al.* 2006) compared to the SA computed from GPS (red dots) and to the SA computed from the strong-motion records (green dots). The error bars indicate the 1σ uncertainty zone of the GMPE.
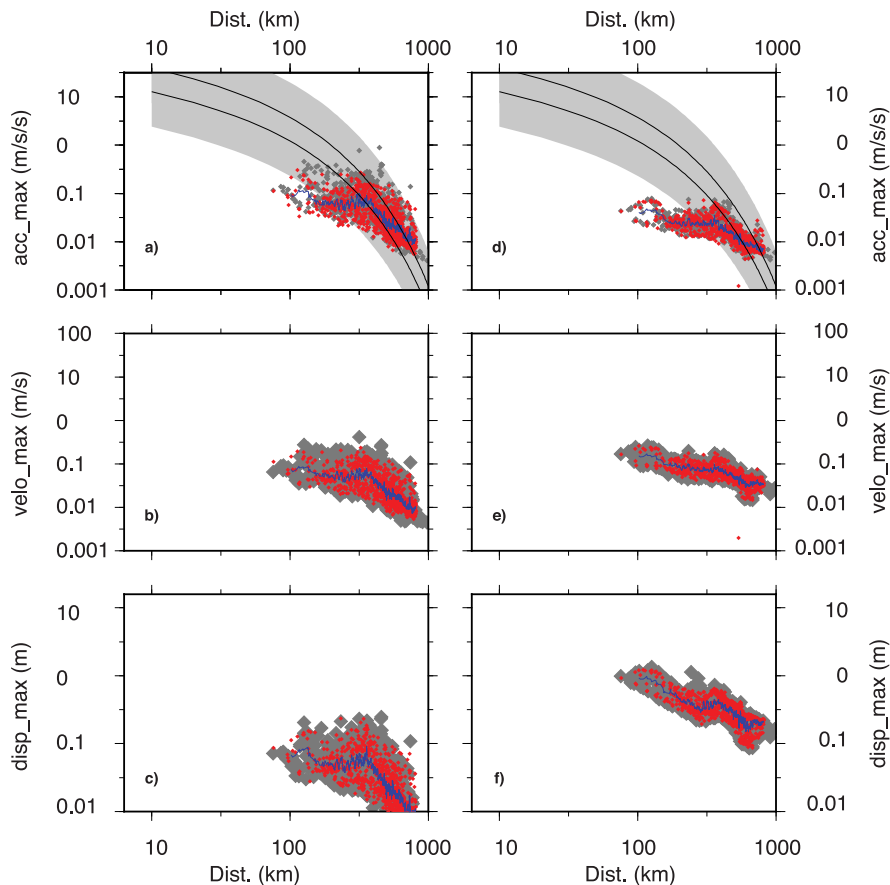

Figure 10. GPS (red) and strong-motion (grey) MGA, MGV and MGD for the 3–10 s (left-hand panel) and 10–100 s (right-hand panel) period bands. The blue curve shows the average GPS MGA/MGV/MGD values.

Fig. 10 shows the strong-motion and GPS maximum accelerations, velocities and displacements of the two period bands (3–10 and 10–100 s) with respect to the distance to the epicentre. The comparison of MGA with GMPE predictions is less relevant as the long-period signals were not used to build the GMPE. For large distances, several values of MGA exceed the estimated PGA predicted by the GMPE. We remind that this discrepancy is however related to small amplitude motions and more interestingly to the response of basins located at distance >200 km. Basins response is however not sufficient to explain the evolution of MGA, MGV and MGD with distance.

Like the accelerations, the maximum displacement estimates depend on the period range. We know that MGD for the short-periods are ∼10 times smaller than for long-periods (at ∼1 m), and we might expect that PGD follows the same trend, so does the PGA. In the case of a single rupture patch, we expect a decay of the form 1/distance in the displacement/distance diagrams. In Fig. 10(f), displaying long-period oscillatory displacements, the displacement versus distance curve does not constantly decrease, but also increases with a second peak at a distance of about 250 km from the epicentre. For better visibility, the averaged displacement for each distance is shown using a blue line. Such a pattern for long-periods (10–100 s) suggests

that the ground motion results from the rupture of two distinct fault segments. The averaged velocity and acceleration is also computed (blue line, Figs 10d and e) but the feature of increment of the two variables is not so pronounced mainly due to the weak velocity and acceleration signal in long-periods.

Regarding the oscillatory acceleration and velocity, they appear to be constant for the short-period (3–10 s) and distance up to 250–300 km from the epicentre (Fig. 10), and then decrease with distance linearly (in a log–log space). This pattern suggests that the strong short-period oscillatory component is generated in an extended rupture area, which seems to cover the location of the two different rupture patches, as it was revealed by the long-period displacement. The plateau cannot be seen clearly in the short-period oscillatory displacements due to the relatively small signal of the corresponding displacements.

Stewart *et al.* (2013) extensively compared GMPEs to the observed ground motion of the Tohoku-Oki event and could not detect the stability of MGA/MGV with increasing distance. Indeed, whereas high-frequency ground motion (intensity measures such as PGA or PGV) is generated by small-scale asperities all along the fault, low-frequency parameters of the ground motion such as displacement is caused by large-scale asperities that may be more localized on the fault as shown by source inversions. These phenomena impact the choice of an optimal distance measure: whereas distance to rupture is the most relevant for high frequencies as used by Stewart *et al.* (2013), distance to major asperities is better for low frequencies. The possibility of the presence of two sources is critical for correct ground motion estimation. Indeed, as the two sources would be shifted relatively to each other, expected ground motion would be larger at larger distances from the first epicentre.

4 CONCLUSIONS AND OUTLOOK

The first conclusion of our work is that both GPS displacement histories and integrated accelerograms are in agreement for the frequency range they have in common (3–100 s). We find that long-period oscillatory ground motions are accurately determined when based on GPS data. The double integration of accelerograms does not impact the precise resolution of the derived displacement data for periods less than 100 s for a large earthquake such as the Tohoku-Oki event.

In future, the PPP GPS data will be processed in near real-time (Branzanti *et al.* 2013) or even real-time (temporal point positioning; Li *et al.* 2013b), allowing the computation of maximum ground motion to supplement other seismic monitoring systems (Liu *et al.* 2014; Tu 2014). Considering that the ground acceleration is expected to be more than five times higher at a period of 1 s than the signal at a period of 10 s, the reliability of the GPS for higher sampling rates (>1 Hz) will mostly depend on our capability to maintain the noise of the time-series at a level close to cm as suggested by Moschas *et al.* (2014).

Cauzzi & Faccioli (2008) demonstrated the importance of accurate GMPEs at long-periods and the limited amount of available seismic data at these periods. We propose that the future generations of GMPEs should include more long-period data such as GPS displacement time-series, in order to better estimate effects of large magnitude ($M_w > 7$) events.

Furthermore, we highlight the response of major sedimentary basins of Japan to the shake that followed the M_w9.0 Tohoku-Oki 2011 earthquake, for periods ranging from 3 to 10 s. The increase in oscillatory displacement at ∼250 km distance from the epicentre

can be interpreted as a second source of displacement along the fault generated by a second asperity as proposed by the source models of Koketsu *et al.* (2011), Suzuki *et al.* (2011) and Maercklin *et al.* (2012). Long-period maximum oscillatory displacement can therefore be used as a constraint for source inversions, providing additional constraints on spatial pattern of rupture at depth.

REFERENCES

Anderson, J.G., Bodin, P., Brune, J.N., Prince, J., Singh, S.K., Quaas, R. & Onãte, M., 1986. Strong ground motion from the Michoacan, Mexico, earthquake, *Science,* **233,** 1043–1049.

Aoi, S., Kunugi, T. & Fujiwara, H., 2004. Strong-motion seismograph network operated by NIED: K-NET and KiK-net, *J. Jpn. Assoc. Earthq. Eng.,* **4**(3), 65–74.

Aoi, S., Kunugi, T., Nakamura, H. & Fujiwara, H., 2011. Deployment of new strong motion seismographs of K-NET and KiK-net, in Earthquake Data in Engineering Seismology, *Geotech. Geol. Earthq. Eng.,* **14,** 167–186.

Assimaki, D., Ledezma, C., Montalva, G.A., Tassara, A., Mylonakis, G. & Boroschek, R., 2012. Site effects and damage patterns, *Earthq. Spectra,* **28**(1), S55–S74.

Avallone, A. *et al.*, 2011. Very high rate (10 Hz) GPS seismology for moderate-magnitude earthquakes: the case of the Mw 6.3 L'Aquila (central Italy) event, *J. geophys. Res.,* **116**(B2), B02305, doi:10.1029/2010JB007834.

Behrens, J., Androsov, A., Babeyko, A., Harig, S., Klaschka, F. & Mentrup, L., 2010. A new multi-sensor approach to simulation assisted tsunami early warning, *Nat. Hazards Earth Syst. Sci.,* **10**(6), 1085–1100.

Blewitt, G., 2008. Fixed point theorems of GPS carrier phase ambiguity resolution and their application to massive network processing: Ambizap, *J. geophys. Res. B: Solid Earth,* **113**(12), B12410, doi:10.1029/2008JB005736.

Blewitt, G., Kreemer, C., Hammond, W.C., Plag, H.-P., Stein, S. & Okal, E., 2006. Rapid determination of Earthquake magnitude using GPS for Tsunami Warning Systems. *Geophys. Res. Lett.,* **33,** L11309, doi:10.1029/2006GL026145.

Blewitt, G., Hammond, W.C., Kreemer, C., Plag, H.-P., Stein, S. & Okal, E., 2009. GPS for real-time earthquake source determination and tsunami warning systems, *J. Geod.,* **83**(3–4), 335–343.

Bock, H., Dach, R., Jäggi, A. & Beutler, G., 2009. High-rate GPS clock corrections from CODE: support of 1 Hz applications, *J. Geod.,* **83**(11), 1083–1094.

Bock, Y., Prawirodirdjo, L. & Melbourne, T., 2004. Detection of arbitrary large dynamic ground motions with a dense high-rate GPS network, *Geophys. Res. Lett.,* **31,** L06604, doi:10.1029/2003GL019150.

Bock, Y., Melgar, D. & Crowell, B., 2011. Real-time strong-motion broadband displacements from collocated GPS and accelerometers, *Bull. seism. Soc. Am.,* **101,** 2904–2925.

Boore, D.M., 2003. Analog-to-digital conversion as a source of drifts in displacements derived from digital recording of ground acceleration, *Bull. seism. Soc. Am.,* **93**(5), 2017–2024.

Branzanti, M., Colosimo, G., Crespi, M. & Mazzoni, A., 2013. GPS near-real-time coseismic displacements for the great Tohoku-Oki earthquake, *IEEE Geosci. Remote Sens. Lett.,* **10**(2), 372–376.

Cauzzi, C. & Faccioli, E., 2008. Broadband (0.05 to 20 s) prediction of displacement response spectra based on worldwide digital records, *J. Seismol.,* **12**(4), 453–475.

Chávez-García, F.J. & Bard, P.-Y., 1994. Site effects in Mexico City eight years after the September 1985 Michoacan earthquakes, *Soil Dyn. Earthq. Eng.,* **13,** 229–247.

Çelebi, M. & Sanli, A., 2002. GPS in pioneering dynamic monitoring of long-period structures, *Earthq. Spectra,* **18**(1), 47–61.

Crowell, B.W., Bock, Y. & Squibb, M.B., 2009. Earthquake early-warning using total displacement waveforms from real-time GPS networks, *Seismol. Res. Lett.,* **80**(5), 772–782.

Dach, R., Hugentobler, U., Meindl, M. & Fridez, P., 2007. *The Bernese GPS Software Version 5.0,* 1st edn, Astronomical Institute, University of Bern.

Dach, R. *et al.,* 2009. GNSS processing at CODE: status report, *J. Geod.,* **83**(3–4), 353–366.

Delouis, B., Nocquet, J.-M. & Vallée, M., 2010. Slip distribution of the February 27, 2010 Mw = 8.8 Maule Earthquake, central Chile, from static and high-rate GPS, InSAR, and broadband teleseismic data, *Geophys. Res. Lett.,* **37,** L17305, doi:10.1029/2010GL043899.

Denolle, M.A., Dunham, E.M., Prieto, G.A. & Beroza, G.C., 2013. Ground motion prediction of realistic earthquake sources using the ambient seismic field, *J. geophys. Res.: Solid Earth,* **118**(5), 2102–2118.

Ducic, V., Artru, J. & Lognonné, P., 2003. Ionospheric remote sensing of the Denali Earthquake Raleigh surface waves, *Geophys. Res. Lett.,* **30**(18), 1951, doi:10.1029/2003GL017812.

Emore, G., Haase, J., Choi, K., Larson, K. & Yamagiwa, A., 2007. Recovering absolute seismic displacements through combined use of 1-Hz GPS and strong motion accelerometers, *Bull. seism. Soc. Am.,* **97,** 357–378.

Feng, L., Newman, A.V., Farmer, G.T., Psimoulis, P. & Stiros, S., 2010. Energetic rupture, coseismic and post-seismic response of the 2008 Mw6.4 Achaia-Elia Earthquake in northwestern Peloponnese, Greece: an indicator of an immature transform fault zone, *Geophys. J. Int.,* **183**(1), 103–110.

Galvan, D.A., Komjathy, A., Hickey, M.P., Stephens, P., Snively, J., Tony Song, Y., Butala, M.D. & Manucci, A.J., 2012. Ionospheric signatures of Tohoku-Oki tsunami of March 11, 2011: model comparisons near the epicenter, *Radio Sci.,* **47**(4), RS4003, doi:10.1029/2012RS005023.

Ge, M., Gendt, G., Rothacher, M., Shi, C. & Liu, J., 2008. Resolution of GPS carrier-phase ambiguities in Precise Point Positioning (PPP) with daily observations, *J. Geod.,* **82**(7), 389–399.

Guo, A., Wang, Y., Li, Z., Ni, S., Wu, W., Liu, G., Zheng, Y. & Simons, M., 2013. Observation of core phase ScS from the mw 9.0 Tohoku-oki earthquake with highrate GPS, *Seismol. Res. Lett.,* **84**(4), 594–599.

Houlié, N., Briole, P., Nercessian, A. & Murakami, M., 2005. Volcanic plume above Mount St. Helens detected with GPS, *EOS, Trans. Am. geophys. Un.,* **86**(30), 277–281.

Houlié, N., Briole, P., Bonforte, A. & Puglisi, G., 2006. Large scale ground deformation of Etna observed by GPS between 1994 and 2001, *Geophys. Res. Lett.,* **339**(2), L02309, doi:10.1029/2005GL024414.

Houlié, N., Occhipinti, G., Shapiro, N., Lognonné, P. & Murakami, M., 2011. New approach to detect seismic surface waves in 1 Hz-sampled GPS time series, *Sci. Rep.,* **1**(44), doi:10.1038/srep00044.

Houlié, N., Dreger, D. & Kim, A., 2014. GPS source solution of the 2004 Parkfield earthquake, *Sci. Rep.,* **4,** 3646, doi:10.1038/srep03646.

Hurter, F., Geiger, A., Perler, D. & Rothacher, M., 2012. GNSS water vapor monitoring in the Swiss Alp, in *Proceedings of the Int. Geosci. Rem. Sens. Symp. (IGARSS),* 2012 IEEE International, doi:10.1109/IGARSS.2012.6351115.

Ji, C., Larson, K., Tan, Y., Hudnut, K. & Choi, K., 2004. Slip history of the 2003 San Simeon earthquake constrained by combining 1-Hz GPS, strong motion, and teleseismic data, *Geophys. Res. Lett.,* **31,** L17608, doi:10.1029/2004GL020448.

Jokinen, A., Feng, S., Schuster, W., Ochieng, W., Hide, C., Moore, T. & Hill, C., 2013. Integrity monitoring of fixed ambiguity Precise Point Positioning (PPP) solutions, *Geosp. Inf. Sci.,* **16**(3), 141–148.

Karia, S., Sarkar, S. & Pathak, K., 2012. Analysis of GPS-based TEC and electron density by the DEMETER satellite before the Sumatra earthquake on 30 September 2009, *Int. J. Remote Sens.,* **33**(16), 5119–5134.

Kobayashi, R., Miyazaki, S. & Koketsu, K., 2006. Source processes of the 2005 West Off Fukuoka Prefecture earthquake and its largest aftershock

inferred from strong motion and 1-Hz GPS data, *Earth Planets Space,* **58,** 57–62.

Koketsu, K. & Miyake, H., 2008. A seismological overview of long-period ground motion, *J. Seismol.,* **12**(2), 133–143.

Koketsu, K. *et al.,* 2011. A unified source model for the 2011 Tohoku earthquake, *Earth planet. Sci. Lett.,* **310,** 480–487.

Larson, K., Bodin, P. & Gomberg, J., 2003. Using 1-Hz GPS data to measure deformations caused by the Denali fault earthquake, *Science,* **300,** 1421–1424.

Lermo, J. & Chavez-Garcia, F.J., 1994. Site effect evaluation at Mexico City: dominant period and relative amplification from strong motion and microtremor records, *Soil Dyn. Earthq. Eng.,* **13,** 413–423.

Li, X., Ge, M., Zhang, Y., Wang, R., Xu, P., Wickert, J. & Shuh, H., 2013a. New approach for earthquake/tsunami monitoring using dense GPS networks, *Sci. Rep.,* **3,** doi:10.1038/srep02682.

Li, X., Ge, M., Guo, B., Wickert, J. & Schuh, H., 2013b. Temporal Point Positioning approach for real-time GNSS seismology using a single receiver, *Geoph. Res. Lett.,* **40**(21), 5677–5682.

Liu, Z., Owen, S. & Moore, A., 2014. Rapid estimate modeling of permanent coseismic displacements for large earthquakes using high-rate global positioning system data, *Seismol. Res. Lett.,* **85**(2), 284–294.

Maercklin, N., Festa, G., Colombelli, S. & Zollo, A., 2012. Twin ruptures grew to built up the giant 2011 Tohoku, Japan, earthquake, *Sci. Rep.,* **709**(2), 1–7.

Margaris, B. *et al.,* 2010. The 8 June 2008 Mw6.5 Achaia-Elia, Greece earthquake: source characteristics, ground motions, and ground failure, **26**(2), 399–424.

Mai, C.-L. & Kian, J.-F., 2009. Reconstruction of ionospheric perturbation induced by 2004 sumatra tsunami using computerized tomography technique, *IEEE Trans. Geosci. Remote Sens.,* **47**(10), **4,** 3303–3312.

Mamula, L., Kudo, K. & Shima, E., 1984. Distribution of ground-motion amplification factors as a function of period (3–15 sec), in Japan, *Bull. Earthq. Res. Inst.,* **59,** 467–500.

Melgar, D., Brendan, W.C., Bock, Y. & Haase, J.S., 2013. Rapid modelling of the 2011 Mw 9.0 Tohoku-oki earthquake with seismogeodesy, *Geophys. Res. Lett.,* **40,** 2963–2968.

Meng, G., Ren, J., Su, X., Yang, Y., Zhu, Z., Ge, L. & Li, X., 2013. Coseismic deformation of the 2010 Mw 6.9 Yushu earthquake derived from GPS data, *Seismol. Res. Lett.,* **84**(1), 57–64.

Mitsui, Y. & Heki, K., 2012. Observation of Earth's free oscillation by dense GPS array: after the 2011 Tohoku megathrust earthquake, *Sci. Rep.,* **2**(931), doi:10.1038/srep00931.

Miyazaki, S. *et al.,* 2004. Modeling the rupture process of the 2003 September 25 Tokachi-Oki (Hokkaido) earthquake using 1-Hz GPS data, *Geophys. Res. Lett.,* **31,** L21603, doi:10.1029/2004GL021457.

Moschas, F., Avallone, A., Saltogianni, N. & Stiros, S., 2014. Strong-motion displacement waveforms using 10-Hz precise point positioning GPS: an assessment based on free oscillation experiments, *Earthq. Eng. Struct. Dyn.,* doi:10.1002/eqe.2426.

Newman, A.V. *et al.,* 2012. Recent geodetic unrest at Santorini Caldera, Greece, *Geophys. Res. Lett.,* **39**(6), L06309, doi:10.1029/2012GL051286.

Ohta, Y., Meiano, I., Sagiya, T., Kimata, F. & Hirahara, K., 2006. Large surface wave of the 2004 Sumatra-Andaman earthquake captured by the very long baseline kinematic analysis of 1-Hz GPS data, *Earth Planet Space,* **58,** 153–157.

Ohta, Y. *et al.,* 2012. Quasi real-time fault model estimation for near-field tsunami forecasting based on RTK-GPS analysis: application to the 2011 Tohoku-Oki earthquake (M_w9.0), *J. geophys. Res.,* **117,** B02311, doi:10.1029/2011JB008750.

O'Toole, T.B., Valentine, A.P. & Woodhouse, J.H., 2012. Centroid-moment tensor inversions using high-rate GPS waveforms, *Geophys. J. Int.,* **187**(3), 1516–1536.

O'Toole, T.B., Valentine, A.P. & Woodhouse, J.H., 2013. Earthquake source parameters from GPS-measured static displacements with potential for real-time application, *Geophys. Res. Lett.,* **40**(1), 60–65.

Perler, D., Geiger, A. & Hurter, F., 2011. GPS water vapour tomography: new parameterized approaches, *J. Geod.,* **85**(8), 539–550.

Psimoulis, P. & Stiros, S., 2008. Experimental assessment of the accuracy of GPS and RTS for the determination of the parameters of oscillation of major structures, *Comput.-Aided Civil Infrastruct. Eng.,* **23**(5), 389–403.

Psimoulis, P. & Stiros, S., 2012. A supervised learning computer-based algorithm to derive the algorithm of oscillations of structures using noisy GPS and Robotic Theodolites (RTS) records, *J. Comput. Struct.,* **92–93,** 337–348.

Psimoulis, P., Pytharouli, S., Karambali, D. & Stiros, S., 2008. Potential of Global Positioning System (GPS) to measure frequencies of oscillations of engineering structures, *J. Sound Vibrat.,* **318**(3), 606–623.

Psimoulis, P., Houlié, N., Meindl, M. & Rothacher, M., 2015. Consistency of GPS and strong-motion records: case study of Mw9.0 Tohoku-Oki 2011 earthquake, *Smart Struct. Syst.,* **26,** accepted.

Roten, D., Olsen, K.B., Pechmann, J.C., Cruz-Atienza, V.M. & Magistrale, H., 2011. 3D simulations of M7 earthquakes on the Wasatch fault, Utah. Part I: long-period (0–1 Hz) groung motion, *Bull. seism. Soc. Am.,* **101**(5), 2045–2063.

Roten, D., Miyake, H. & Koketsu, K., 2012. A Rayleigh wave back-projection method applied to the 2011 Tohoku earthquake, *Geophys. Res. Lett.,* **39,** L02302, doi:10.1029/2011GL050183.

Sagiya, T., 2004. A decade of GEONET: 1994–2003—the continuous GPS observation in Japan and its impact on earthquake studies, *Earth Planet Space,* **56,** xxix–xli.

Singh, S.K., Mena, E. & Castro, R., 1988. Some aspects of source characteristics of the 19 September 1985 Michoacan earthquake, and ground motion amplifications in and near Mexico City from strong motion data, *Bull. seism. Soc. Am.,* **78,** 451–477.

Sobolev, S.V. *et al.*, 2007. Tsunami early warning using GPS-Shield arrays, *J. geophys. Res.,* **112,** B08415, doi:10.1029/2006JB004640.

Stewart, J.P., Midorikawa, S., Graves, R.W., Khodaverdi, K., Kishida, T., Miura, H. & Campbell, K.W., 2013. Implications of the M w 9.0 Tohoku-Oki Earthquake for Ground Motion Scaling with Source, Path, and Site Parameters, *Earthq. Spectra,* **29**(S1), S1–S21.

Stiros, S., 2008. Errors in velocities and displacements deduced from accelerographs: an approach based on the theory of error propagation, *Soil Dyn. Earthq. Eng.,* **28,** 415–420.

Suzuki, W., Aoi, S., Sekiguchi, H. & Kunugi, T., 2011. Rupture process of the 2011 Tohoku-Oki megathrust earthquake (M9.0) inverted from strong-motion data, *Geophys. Res. Lett.,* **38,** L00G16, doi:10.1029/2011GL049136.

Tu, R., 2014. Fast determination of displacement by PPP velocity estimation, *Geophys. J. Int.,* **196**(3), 1397–1401.

Vigny, C. *et al.*, 2005. Insight into the 2004 Sumatra-Andaman earthquake from GPS measurements in southeast Asia, *Nature,* **436,** 201–206.

Wang, G., Boore, D. M., Tang, G. & Zhou, X., 2007. Comparisons of ground motions from collocated and closely spaced one-sample-per-second Global Positioning System and accelerograph recordings of the 2003M6.5 San Simeon, California, earthquake in the Parkfield Region, *Bull. seism. Soc. Am.,* **97**(1B), 76–90.

Wright, T., Houlié, N., Hildyard, M. & Iwabuchi, T., 2012. Real-time, reliable magnitude for large earthquakes from 1Hz GPS precise point positioning: the 2011 Tohoku-Oki (Japan) earthquake, *Geophys. Res. Lett.,* **39,** L12302, doi:10.1029/2012GL051894.

Yagi, Y. & Fukahata, Y., 2011. Rupture process of the 2011 Tohoku-oki earthquake and absolute elastic strain release, *Geophys. Res. Lett.,* **38**(19), L19307, doi:10.1029/2011GL048701.

Yamanaka, H., Seo, K. & Samano, T., 1989. Effects of sedimentary layers on surface-wae propagation, *Bull seism. Soc. Am.,* **79**(3), 631–644.

Yokota, Y., Koketsu, K., Hikima, K. & Miyazaki, S., 2009. Ability of 1-Hz GPS data to infer the source process of a medium-sized earthquake: the case of the 2008 Iwate-Miyagi Nairiku, Japan, earthquake, *Geophys. Res. Lett.,* **36,** L12301, doi:10.1029/2009GL037799.

Yue, H. & Lay, T., 2011. Inversion of high-rate (1sps) GPS data for rupture process of the 11 March 2011 Tohoku earthquake (M_w9.1), *Geophys. Res. Let.,* **38,** L00G09, doi:10.1029/2011GL048700.

Zhao, J.X. *et al.*, 2006. Attenuation relations of strong ground motion in Japan using site classification based on predominant period, *Bull seism. Soc. Am.,* **96,** 898–913.
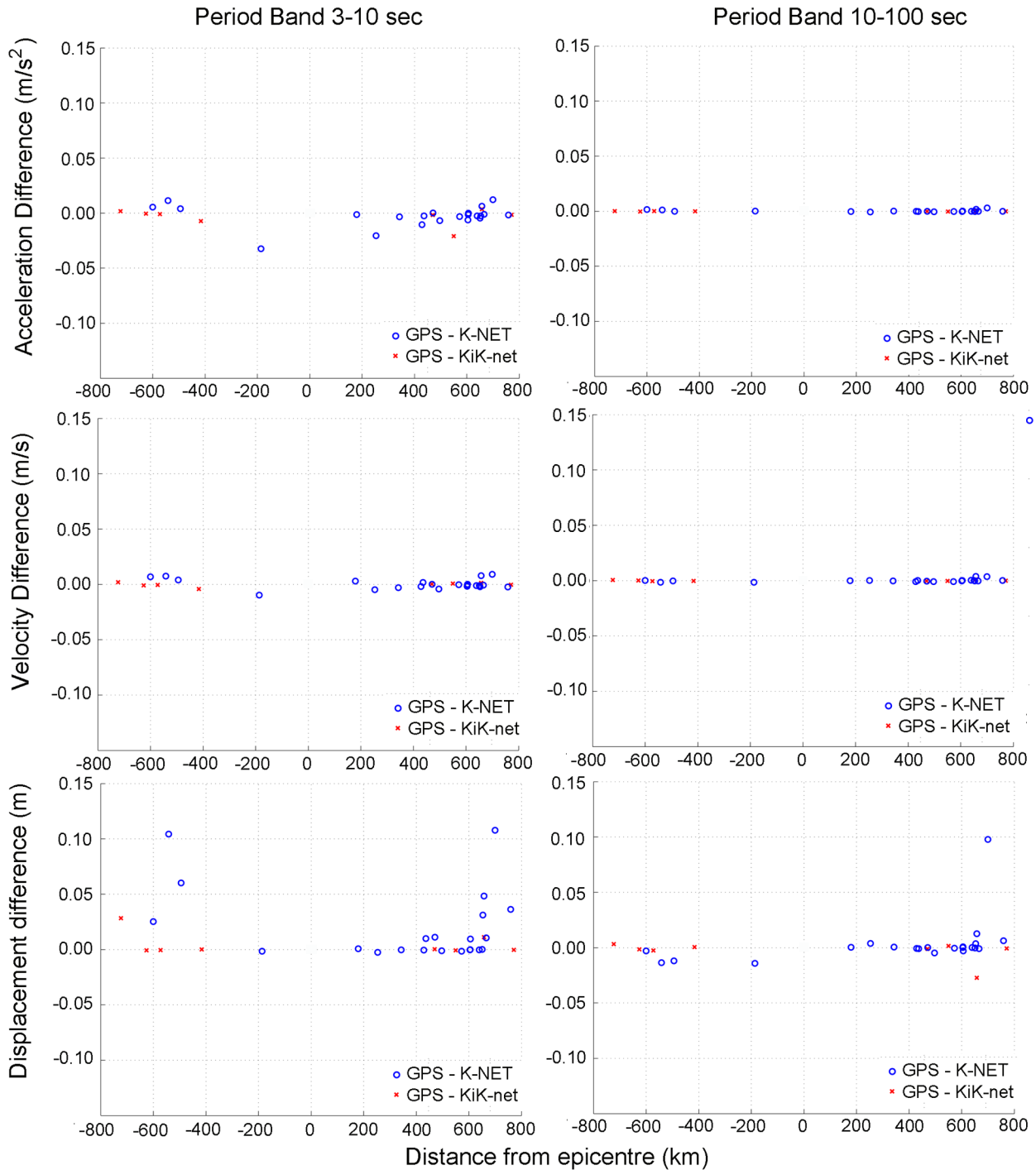
APPENDIX

Figure A1. The differences of the GPS and strong-motion MGA (top panel), MGV (middle panel) and MGD (bottom panel) values for each very closely located sites versus the distance from the epicentre. The positive and negative distances correspond to the position of the sites northward and southward from the epicentre.